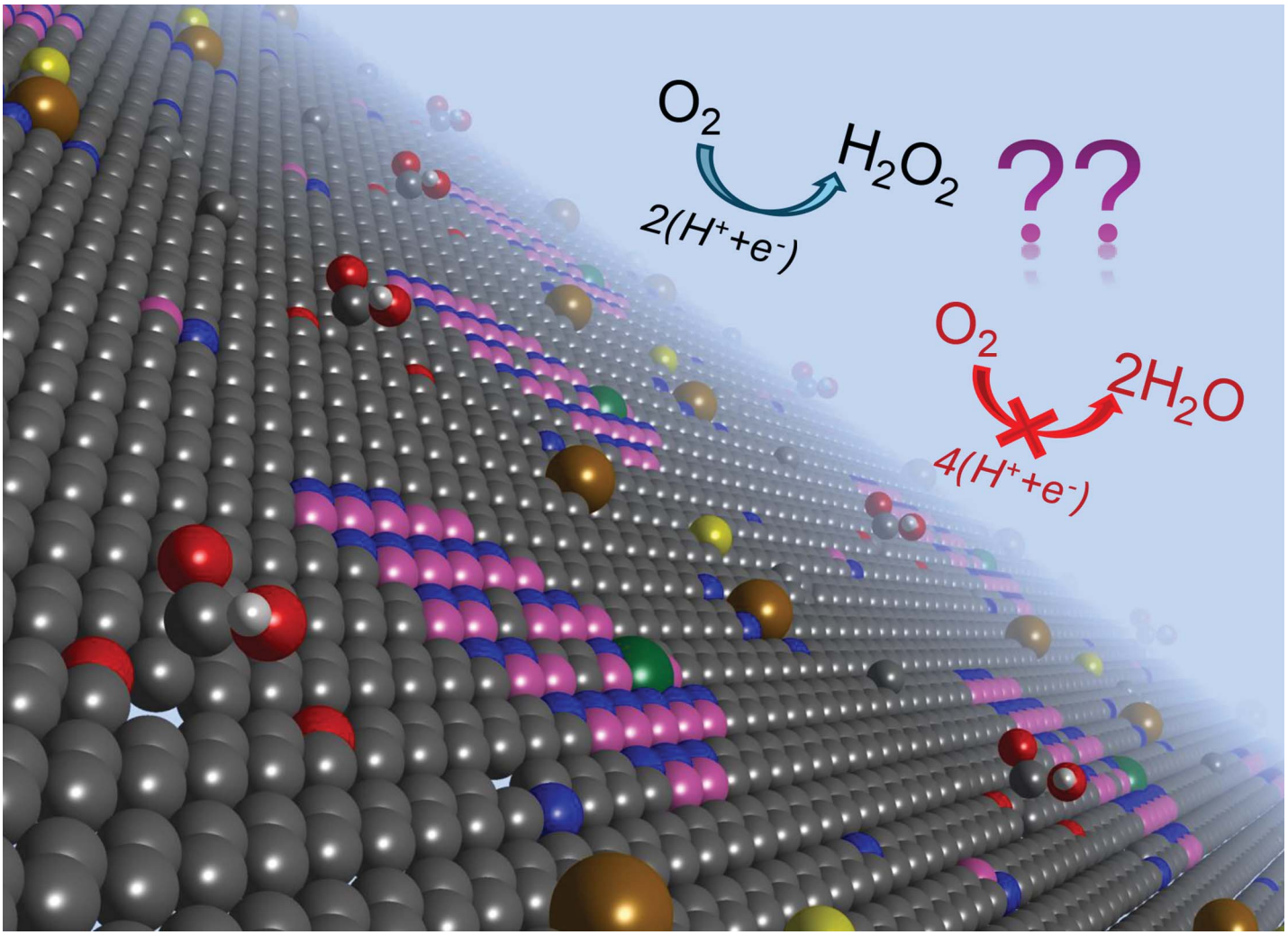

Showcasing research from Professor Samira Siahrostami's laboratory, Department of Chemistry, Simon Fraser University, British Columbia, Canada.

Selectivity trends in two-electron oxygen reduction: insights from two-dimensional materials

This work explores selectivity trends in the two-electron oxygen reduction reaction (2e-ORR) across a broad set of two-dimensional (2D) materials. By systematically analysing active sites and employing the descriptor ΔΔG, the study reveals how structural and electronic features govern selectivity toward hydrogen peroxide production. The findings highlight that not all catalytically active sites exhibit high selectivity, underscoring the importance of distinguishing activity from product preference. These insights provide valuable design principles for identifying and engineering 2D catalysts optimized for efficient 2e-ORR.

Image reproduced by permission of Samira Siahrostami from *Chem. Sci.*, 2025, **16**, 15926.

As featured in:

See Samira Siahrostami, *Chem. Sci.*, 2025, **16**, 15926.

ROYAL SOCIETY OF CHEMISTRY

15 YEARS ANNIVERSARY

rsc.li/chemical-science

Registered charity number: 207890

Chemical Science

ROYAL SOCIETY OF CHEMISTRY

EDGE ARTICLE

View Article Online
View Journal | View Issue

Cite this: *Chem. Sci.*, 2025, **16**, 15926

All publication charges for this article have been paid for by the Royal Society of Chemistry

Received 3rd July 2025
Accepted 4th August 2025

DOI: 10.1039/d5sc04904k

rsc.li/chemical-science

Selectivity trends in two-electron oxygen reduction: insights from two-dimensional materials

Samira Siahrostami *

Advancing the discovery of novel materials for electrosynthesis of hydrogen peroxide (H_2O_2) *via* the two-electron oxygen reduction reaction (2e-ORR) while rationalizing and quantifying selectivity trends has been an ambitious objective. A recently introduced selectivity descriptor, $\Delta\Delta G$, published in *Chem Catal.* 2023, 3(3), 100568, utilizes thermodynamic analysis of adsorption free energies of key ORR intermediates (ΔG_{OOH*} and ΔG_{O*}) along with the free energy of H_2O_2 to quantify selectivity and establish trends. This model has been successfully applied to a large database of binary alloys, demonstrating strong potential for predicting selective materials *Angew. Chem. Int. Ed.* 2024, 63, e202404677. In this study, we systematically explore a diverse range of active sites in carbon-based structures, boron nitrides, and single atom catalysts, emerging classes of materials for 2e-ORR. We assess the effectiveness of $\Delta\Delta G$ in capturing selectivity trends and distinguishing sites that are both catalytically active and highly selective. Our findings highlight that not all active sites in carbon-based materials reported with high activity inherently exhibit high selectivity, with only a small fraction meeting both criteria. This work highlights the importance of $\Delta\Delta G$ as a predictive tool, providing valuable insights for designing selective and active two-dimensional materials.

Introduction

The two-electron oxygen reduction reaction (2e-ORR) has attracted significant attention in both experimental and computational research due to its ability to produce hydrogen peroxide (H_2O_2) *via* the electrochemical reduction of oxygen without a need for energy input. H_2O_2 is a versatile chemical with a wide range of applications in energy and environmental sectors, including electronics, metallurgy, pulp and paper bleaching, textiles, propylene oxide production, detergents, wastewater treatment, and sanitation. Furthermore, H_2O_2 holds potential for use in energy storage systems, particularly in conjunction with renewable energy sources. As a powerful oxidizing agent, H_2O_2 offers advantages such as superior performance over chlorine in water treatment, as it breaks down into harmless water and oxygen, leaving no toxic byproducts.[1]

The main industrial method for H_2O_2 production, the anthraquinone process, meets current global demand but its energy-intensive multi-step process requires high energy input, as well as costly noble metal catalysts.[1] Additionally, the process generates large amounts of waste, including toxic organic solvents. Furthermore, the produced H_2O_2 must undergo purification, storage, and transportation, all of which contribute to its high cost and environmental footprint.[1] These challenges have sparked considerable interest in direct hydrogen peroxide synthesis (DHSP) *via* electrochemical methods.[2,3] This approach could enable H_2O_2 production under ambient conditions, using renewable energy sources rather than fossil fuels, and green reactants like water and air, instead of the toxic anthraquinone derivatives. As a result, there is growing research into new materials that can efficiently catalyze the 2e-ORR for this purpose.

A major challenge in catalyst development for DHSP is creating cost-effective, durable materials that maximize both activity and selectivity for the 2e-ORR pathway, while minimizing competition with four electron oxygen reduction (4e-ORR) pathway.[4] Selectivity refers to the catalyst's preference for a particular reaction pathway, while activity refers to the rate at which the catalyst facilitates the desired 2e-ORR pathway. Computational tools, particularly density functional theory (DFT) combined with the computational hydrogen electrode (CHE) model[5] and thermodynamic analysis, have proven invaluable in understanding the mechanisms of both 2e-ORR and 4e-ORR, guiding the design of more active catalysts.[6] Based on the computational understanding, adsorption free energy of OOH*, has been proposed as a descriptor to capture and predict trends in catalytic activity toward 2e-ORR[6–8] based of which the state-of-the-art Hg-based alloys[4,9] were discovered. This descriptor-based analysis which is based on thermodynamics of the reaction (dealing with adsorption energy of ORR intermediates as activity descriptors) has proven to be essential in understanding the activity trends and providing guidelines

Department of Chemistry, Simon Fraser University, 8888 University Drive, Burnaby, B.C. V5A 1S6, Canada. E-mail: ssiahros@sfu.ca

for targeted materials with high activity toward electrosynthesis of H_2O_2 thus far.[10–18]

Using this approach, various classes of materials—including carbon-based materials,[10,19–27] metal oxides,[28,29] and metal sulfides[30]—have been extensively studied as potential electrocatalysts for the 2e-ORR. Among these, carbon-based materials have attracted significant interest due to their cost-effectiveness, safety, ease of synthesis, tunability, and wide availability.[10,13,17,19–25,31–34] Additionally, their structural versatility allows for the incorporation of heteroatoms (such as nitrogen, sulfur, and boron), which can modulate electronic properties and enhance catalytic activity. Various studies have also highlighted the role of defect, edge sites, surface functionalization and transition metal doping in optimizing carbon-based materials selectivity and activity for 2e-ORR.[12,35,36]

Various computational studies have demonstrated that thermodynamic analysis and the CHE approach are valuable tools for understanding activity trends and guiding the identification and design of novel materials for the 2e-ORR.[6,22,37–39] On the other hand, selectivity in the 2e-ORR presents a significant challenge. Highly selective materials tend to bind O_2 weakly, preserving the O–O bond and preventing its cleavage upon formation of OOH*, which enhances H_2O_2 production. However, this weak binding also results in low catalytic activity. It is well known that maximizing selectivity often comes at the expense of activity, creating a trade-off between the two properties. To overcome this negative correlation, it is essential to identify materials that can bind O_2 and the associated OOH* intermediate with sufficient strength while still avoiding bond cleavage. This requires strategies such as optimizing the geometric arrangements of surface atoms—for example, through the use of isolated active sites[4]—or by breaking the scaling relationship between adsorbed OOH* and O*, although achieving the latter has proven to be extremely challenging. Furthermore, the absence of a robust metric for quantifying selectivity has hindered the ability to rationalize trends and identify materials that exhibit both high selectivity and catalytic activity. Recently, the introduction of the thermodynamic parameter $\Delta\Delta G$ has addressed this gap by enabling the quantification of selectivity based on the predicted adsorption free energies of ORR intermediates (ΔG_{OOH^*} and ΔG_{O^*}) and the free energy of H_2O_2, as demonstrated in the study by Siahrostami *et al.*[37] This parameter was systematically examined across a broad spectrum of binary alloys, revealing that only a limited number of single-site binary alloys reported for high activity also exhibit high selectivity for 2e-ORR.[40] These selective single-site alloys achieved high 2e-ORR performance through the ensemble effect, effectively overcoming the limitations imposed by the scaling relationship between ΔG_{OOH^*} and ΔG_{O^*}, a phenomenon well captured by $\Delta\Delta G$.

Building upon this prior study, herein we extend the scope of analysis to systematically examine a wide range of active sites in carbon-based structures as well as other two-dimensional materials, including boron nitride and silicon carbide, for the two-electron oxygen reduction reaction (2e-ORR). What distinguishes this work is the comprehensive mapping of both activity and selectivity across diverse material classes using the $\Delta\Delta G$ descriptor. We critically assess the efficacy of $\Delta\Delta G$ not only in capturing selectivity trends, but also in pinpointing active sites that achieve the rare combination of high catalytic activity and high selectivity for 2e-ORR.

Importantly, our study reveals that many active sites previously reported as highly active do not inherently display favorable selectivity, challenging assumptions often made in the field. We demonstrate that only a small subset of these sites achieves both high activity and high selectivity, underscoring the importance of dual-criterion screening for rational catalyst design. This work, therefore, provides a deeper mechanistic understanding and a more rigorous framework for identifying promising 2e-ORR catalysts, particularly among low-cost and earth-abundant two-dimensional materials that have attracted significant attention for sustainable H_2O_2 electrosynthesis.

Computational details

The simulations were carried out using the Atomic Simulation Environment (ASE),[41] with electronic structure calculations performed using the QUANTUM ESPRESSO[42] package. Plane-wave basis sets were used to expand the electronic wave-functions with a cutoff energy of 500 eV, while the electron density was represented on a grid with a cutoff of 5000 eV. Core electrons were modeled using ultrasoft pseudopotentials. The BEEF-vdW exchange-correlation functional[43,44] was employed, as it has been shown to accurately capture both chemisorption and physisorption properties, particularly on graphene and other two-dimensional materials. All structures were modeled as single-layer graphene slabs with supercells ranging from 4×4 to 8×8 in lateral dimensions. The Brillouin zone was sampled using Monkhorst–Pack grids of $(4 \times 4 \times 1)$ and $(2 \times 2 \times 1)$, and a vacuum spacing of approximately 20 Å was added to prevent interactions between periodic images. The computational hydrogen electrode (CHE) approach was used to relate the chemical potential of a proton–electron pair to that of gas-phase H_2 at an electrode potential $U_{elec} = 0.0$ V *vs.* the reversible hydrogen electrode (RHE). The effect of electrode potential on the free energy of reaction intermediates was accounted for by shifting the electron energy by $-eU_{elec}$, where e is the charge and U_{elec} is the applied potential. The calculated zero-point energy (ZPE) and entropy (TS) corrections at standard conditions ($T = 298.15$ K, $p = 1$ bar) for O*, *OH and *OOH are listed in the Supplementary Note 1.

Results and discussion

Various types of active sites on carbon-based materials have been extensively studied, including heteroatom doping, metal doping, oxygen functional groups, defects, and edge sites.[10,19–21,32–34] These structural modifications have been computationally investigated to unravel catalytic activity and selectivity for the 2e-ORR and among these strategies, many have been experimentally validated as active and selective.[20,31,32] For example, studies on oxygen functional groups in partially or fully oxidized carbon structures, such as graphene oxides, have demonstrated that ether, epoxy, and carboxyl groups at carbon

edge sites play a crucial role in promoting H_2O_2 production.[16,17,45,46] Additionally, heteroatom doping (*e.g.*, nitrogen, and boron) has been shown to modulate the electronic structure and influence both activity and selectivity, while metal doping can introduce localized active centers that further optimize performance.[19,20,32,47]

In this study, we compiled a database by conducting and gathering a variety of DFT calculations for ΔG_{OOH*}, ΔG_{O*} and ΔG_{OH*} on two dimensional materials mostly graphene and boron nitride. We then analyze these data to systematically evaluate the impact of these various active sites and gain deeper insights into the underlying selectivity trends for 2e-ORR. Fig. 1 presents the schematics of some of the active sites examined in this study which encompass various types and quantities of N-doping, defects, N-doped defects, and metal-doped graphene (M = Cu, Mo, Pt, Fe, Ag). They also include other heteroatom dopants (P, S, F, Al, B, Cl, Si), various amount of BN co-doping, metal-doped BN (M = Ru, Co, Pt, Ag, Ni, Fe, Pd, Rh, Cu, Os, Mo, Ir), and oxygen functional groups. The calculated and compiled adsorption energy values for ORR intermediates, along with the corresponding references, are provided in SI Tables S1–S4.

As mentioned above, a major challenge in catalyst design for 2e-ORR lies in balancing activity and selectivity. The previous study on binary metal alloys shows that overcoming the inherent scaling relationship between OOH* and O* is crucial for developing highly selective and active catalysts.[40] An ideal catalyst should exhibit both high selectivity and activity. The catalytic activity of the 2e-ORR is assessed by calculating the overpotential (η) based on ΔG_{OOH*}. The η value is calculated using the equation $|\Delta G_{OOH*} - 4.22\ eV|/e$, where 4.22 eV represents the OOH* binding energy of an ideal catalyst with zero overpotential. A lower η indicates higher catalytic activity (Fig. 2).

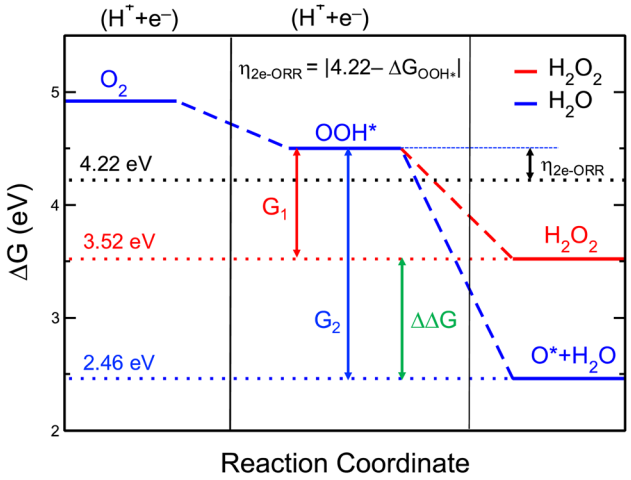

Fig. 2 Free energy diagram for 2e-ORR, illustrating the catalytic activity ($\eta_{2e\text{-}ORR}$) and selectivity ($\Delta\Delta G$) descriptors. Vertical black solid lines represent the steps of coupled proton–electron transfer. Black, red, and blue dotted lines represent the adsorption energy of the OOH* intermediate for an ideal 2e-ORR catalyst, the free energy of H_2O_2 in aqueous solution, and the adsorption energy of O* for an ideal 4e-ORR catalyst, respectively.

To predict the selectivity toward H_2O_2, we utilized the thermodynamic descriptor $\Delta\Delta G$.[37] This descriptor is derived from ΔG_{OOH*} and ΔG_{O*}, condensing the selectivity prediction into a single metric (eqn (1)–(3)). The $\Delta\Delta G$ value is calculated as the difference between G_1 and G_2, which represent the free energy differences between OOH* and its further reduced products, H_2O_2 or O* + H_2O, respectively. Maximum selectivity for the 2e-ORR is achieved when $\Delta\Delta G$ approaches zero (Fig. 2).

$$G_1 = \Delta G_{H_2O_2} - \Delta G_{OOH*} \quad (1)$$

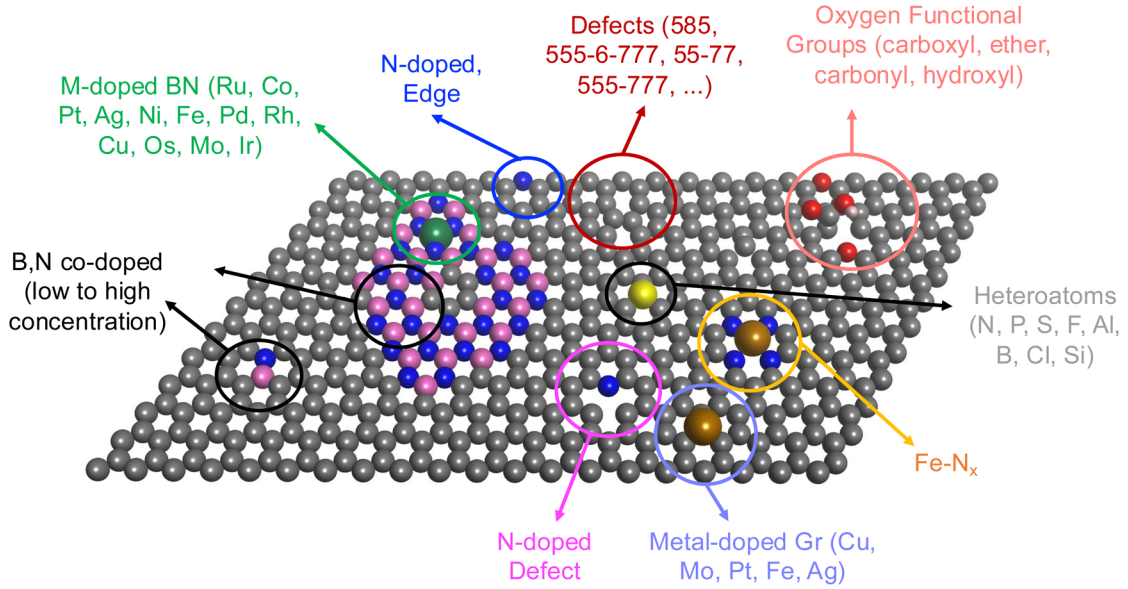

Fig. 1 Schematics of the active sites examined in this study as well as those reported in the literature for their high activity and selectivity toward 2e-ORR. The corresponding calculated and compiled adsorption energy values for ORR intermediates and relevant references are included in Tables S1–S4.

$$G_2 = \Delta G_{O^*+H_2O} - \Delta G_{OOH^*} \quad (2)$$

$$\Delta\Delta G = G_1 - G_2 \quad (3)$$

Substituting G_1 and G_2 in eqn (3) results in:

$$\Delta\Delta G = \Delta G_{H_2O_2} - \Delta G_{O^*+H_2O} \quad (4)$$

For over a decade, ΔG_{OOH^*} has been widely used as a descriptor for both the activity and selectivity of catalysts toward the 2e-ORR.[37] However, recent studies by Siahrostami *et al.* have shown that ΔG_{OOH^*} offers only a qualitative indication of selectivity and is insufficient for reliably capturing selectivity trends across different catalysts.[37,40] For instance, relying solely on ΔG_{OOH^*} as a descriptor of selectivity would categorize all catalysts with $\Delta G_{OOH^*} \sim 4.22$ eV as selective for H_2O_2 production, but this approach overlooks important trends in selectivity.[37,40] Moreover, these studies have shown that selectivity, as quantified by $\Delta\Delta G$, is not dependent on ΔG_{OOH^*} but rather on ΔG_{O^*}, which plays a crucial role in the O–O bond dissociation process.[37,40] It is worth noting that although ΔG_{OOH^*} is included in the definitions of both G_1 (eqn (1)) and G_2 (eqn (2)), it naturally cancels out in the derivation of $\Delta\Delta G$ (eqn (4)), highlighting that ΔG_{O^*} has a more direct and significant influence on selectivity.[37] The application of $\Delta\Delta G$ is especially valuable when screening large datasets where traditional scaling relations break down.[40] As such, $\Delta\Delta G$ offers a more robust and comprehensive selectivity metric that compensates for the limitations of ΔG_{OOH^*} and better captures the influence of key intermediates on catalytic selectivity.

To employ $\Delta\Delta G$ as a descriptor for uncovering selectivity trends in two-dimensional materials, we begin by analyzing the scaling relations within our dataset (Fig. 3a–d). As anticipated, the points are dispersed across all three scaling plots (Fig. 3a–c), suggesting no meaningful scaling behavior when considering various two-dimensional catalysts. The correlation is stronger in Fig. 3b for ΔG_{OOH^*} *vs.* ΔG_{OH^*}, where both intermediates are expected to form single bonds to the active sites. The deviations indicate cases where the OOH* intermediate adopts a bidentate coordination or dissociates into OH* + O.

The weaker correlations observed in Fig. 3a and c result from the generally lower correlation between oxygen species such as O* and OH* or O* and OOH*, which arises from differences in the bond orders they form with the active site. These weak correlations, however, have been proven advantageous for selectivity toward the 2e-ORR, as they provide more flexibility in identifying catalysts that are not only active but also selective for the 2e-ORR.[40] This is because, as discussed above, under the thermodynamic definition (eqn (1)–(4)), 2e-ORR selectivity, $\Delta\Delta G$, is determined by the ΔG_{O^*} (eqn (4)), while 2e-ORR activity is governed by the ΔG_{OOH^*}.

Fig. 3d displays G_1 and G_2 as a function of ΔG_{OH^*}. The difference between G_1 and G_2 for each data point refers to $\Delta\Delta G$ (eqn (3)), a quantitative measure for 2e-ORR selectivity. A smaller $\Delta\Delta G$ value corresponds to a higher 2e-ORR selectivity, with the maximum selectivity being achieved when $\Delta\Delta G$ is zero.

We note the scaling relationships in Fig. 3, such as those between *OH and *OOH or *OH and *O, are subject to inherent uncertainties arising from both the choice of exchange-correlation functional (BEEF-vdW) and the statistical scatter of the data. BEEF-vdW provides an internal estimate of functional uncertainty (0.2–0.3 eV for systems where dispersion interactions are significant and not fully captured[43]), which we have used to compute confidence intervals for these correlations. Accordingly, the trend lines shown in Fig. 3 represent correlations between binding energies of key ORR intermediates with linear regression fits, while the shaded bands indicate the 95% confidence intervals derived from the ensemble of BEEF-vdW functionals in both X and Y binding energy values. These intervals reflect the expected spread in adsorption energies due to exchange-correlation functional uncertainty and provide a more realistic representation of the reliability of the predicted trends.

Fig. 4a displays the $\Delta\Delta G$ values as a function of ΔG_{OH^*} for various active sites in two-dimensional structures examined in this study, providing insight into the identification of active sites that are both active and selective for 2e-ORR. The black vertical dashed line represents the $\Delta G_{OH^*} = 1.0$ eV (corresponding to $\Delta G_{OOH^*} = 4.22$ eV) of an active catalyst for the 2e-ORR with 2e-ORR overpotential ($\eta_{2e\text{-}ORR}$) equal to zero. Active sites closer to the vertical dashed line indicate high 2e-ORR activity with a lower overpotential (gray arrows). The horizontal green dashed line indicates the $\Delta\Delta G = 0.65$ eV which is the value reported for $PtHg_4$ catalyst,[40] serving as a benchmark for selective catalysts. Catalysts with $\Delta\Delta G = 0.0$ are considered to have maximum selectivity. The green arrow in this figure highlights a direction of increasing the 2e-ORR selectivity.

Fig. 4b combines both catalytic activity and selectivity, evaluated through $\eta_{2e\text{-}ORR}$ and $\Delta\Delta G$, respectively. The optimal catalytic activity and selectivity are achieved when $\eta_{2e\text{-}ORR}$ is 0.0 V and $\Delta\Delta G$ is 0.0 eV. Similar to Fig. 4a, the horizontal green dashed line represents the $\Delta\Delta G$ value for the $PtHg_4$ catalyst, which serves as the threshold for selective catalysts. We also relaxed the stringent criterion for $\eta_{2e\text{-}ORR}$, increasing the overpotential threshold from 0.0 V to 0.20 V. The green-shaded area in Fig. 4b can be considered the "holy grail" for achieving both high selectivity and activity toward 2e-ORR.

To better visualize the similarities and differences among the examined two-dimensional catalysts, we generated a bar chart summarizing all $\Delta\Delta G$ and $\eta_{2e\text{-}ORR}$ (Fig. S1). Fig. 4c highlights the most promising two-dimensional structures, defined as those exhibiting either $\Delta\Delta G \leq 0.65$ eV (marked by the red dashed line) or $\eta_{2e\text{-}ORR} \leq 0.20$ V (marked by the black dashed line). The corresponding atomic structures are displayed in Fig. 4d. This analysis reveals that, unlike binary alloys, identifying two-dimensional catalysts that are both active and selective for the 2e-ORR pathway remains highly challenging. In other words, while it is relatively straightforward to pinpoint active sites with high 2e-ORR activity ($\eta_{2e\text{-}ORR} \leq 0.20$ V, highlighted by the pink boxes)—such as single-atom sites of Pt, Pd, Rh, Co or Fe embedded in two-dimensional substrates—these sites, when assessed for selectivity, typically favor the 4e-ORR pathway over the desired 2e-ORR route. This is consistent

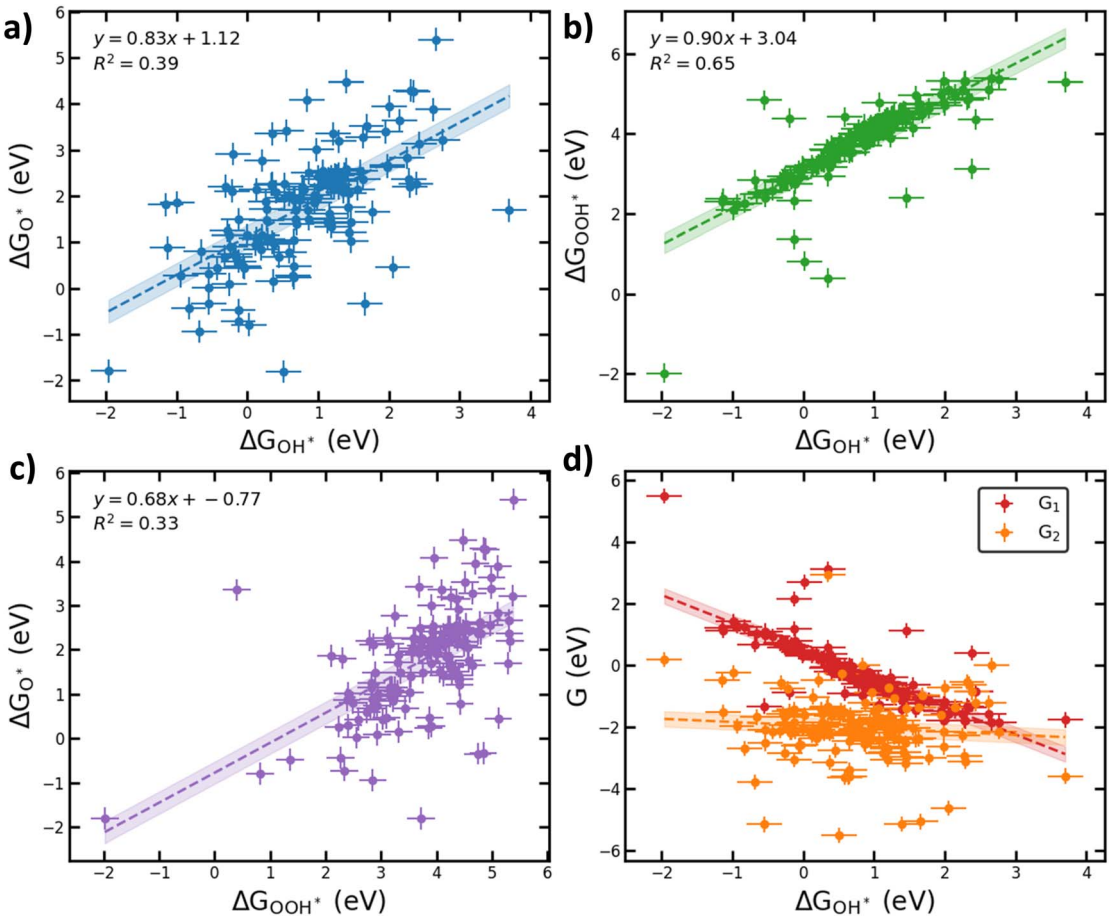

Fig. 3 Correlations between binding energies of key ORR intermediates across our database for two-dimensional materials with linear regression fits: (a) ΔG_{O*} *vs.* ΔG_{OH*}, (b) ΔG_{OOH*} *vs.* ΔG_{OH*}, (c) ΔG_{O*} *vs.* ΔG_{OOH*}, and (d) G_1 and G_2 as a function of ΔG_{OH*}. Shaded bands around the regression lines represent 95% confidence intervals, accounting for the estimated uncertainty (~±0.2–0.3 eV as reported in Ref. 43) in both X and Y binding energy values. Error bars on data points show the individual uncertainties in each datapoint. This visualization explicitly represents the propagation of errors in the correlations.

with various reports, which typically identify these catalysts as efficient 4e-ORR systems.[48–51] Conversely, nearly all active sites with $\Delta\Delta G$ values lower than that of $PtHg_4$ fail to achieve high 2e-ORR activity, indicating that low $\Delta\Delta G$ alone is not a sufficient predictor of catalytic performance for this reaction. This highlights the complex interplay between activity and selectivity in two-dimensional catalysts, where optimizing one property does not necessarily guarantee improvement in the other. It further underscores the need for dual-parameter descriptors or design strategies that can simultaneously balance both activity and selectivity for efficient 2e-ORR catalysis.

As highlighted in green in Fig. 4c, the only active site identified that satisfies both the selectivity and activity criteria is an N-doped single vacancy defect, illustrated in the inset of Fig. 4b. This type of defect is quite common and has a low formation energy, making it highly likely to be present in carbon-based catalysts.[52] We suggest that this could be the active site responsible for the selective and efficient reduction of oxygen to H_2O_2 in metal free N-doped carbon samples.

Notably, recent work by Urrego-Ortiz *et al.*[53] has shown that standard DFT calculations can introduce errors in estimating the absolute energy of H_2O_2. In our study, we mitigate this issue by referencing the experimental free energy of H_2O_2 in our thermodynamic analysis. One could reasonably argue that the computed free energies of *OOH might exhibit similar uncertainties as H_2O_2. However, our focus is on using relative energies to capture screening trends across materials, rather than making absolute quantitative predictions. While uncertainties inherent to GGA-level functionals such as BEEF-vdW may influence absolute values, they have minimal impact on the comparative trends that form the basis of our descriptor-driven insights.

Lastly, we would like to emphasize that the $\Delta\Delta G$ descriptor is derived purely from thermodynamic analysis based on the adsorption free energies of key reaction intermediates involved in the ORR. By construction, it captures intrinsic selectivity trends dictated by the relative stabilities of intermediates on the catalyst surface. However, it does not explicitly account for external factors such as pH, solvent environment, or temperature, all of which are known to influence adsorption energetics and reaction pathways in aqueous electrocatalysis.

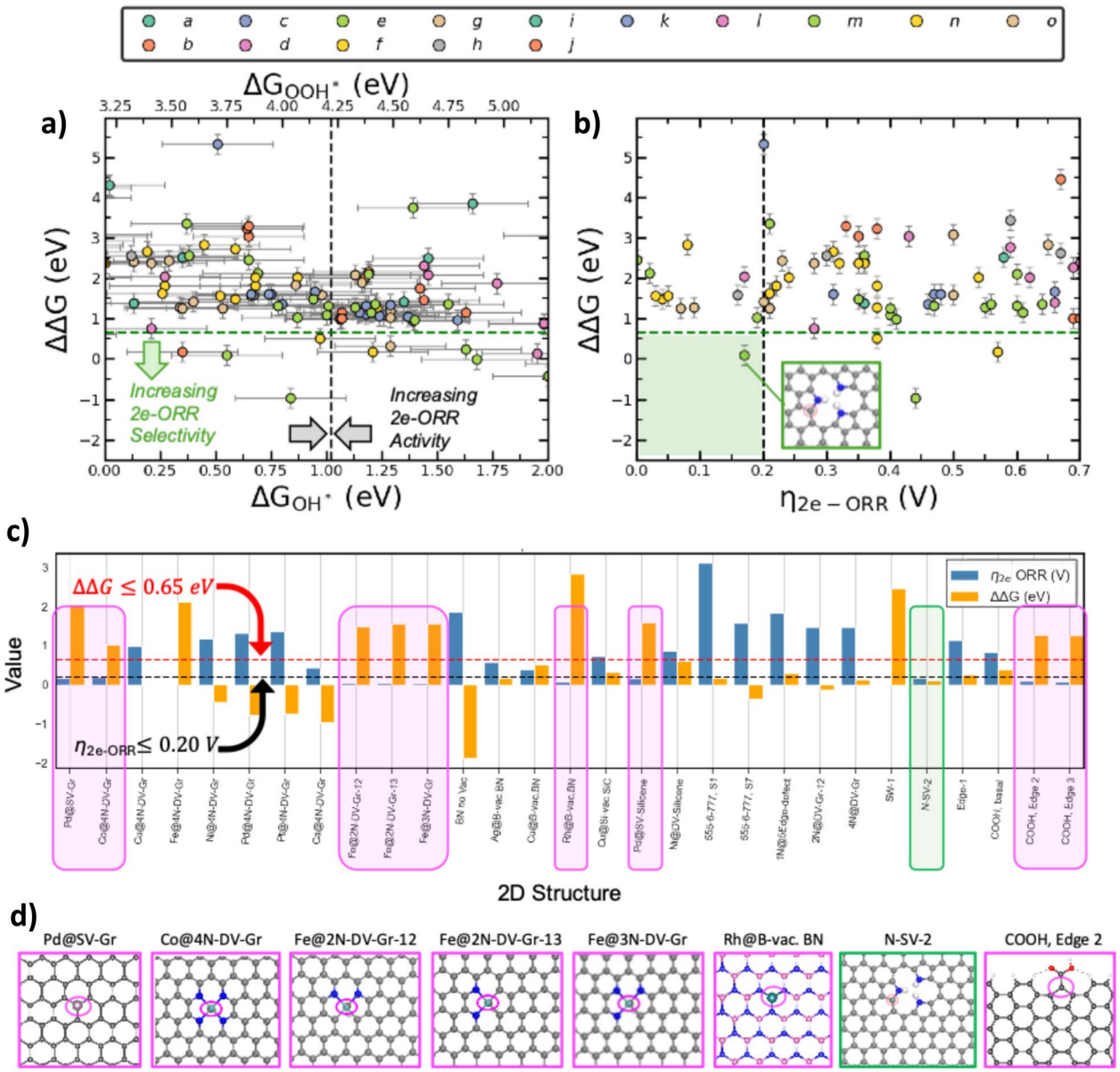

Fig. 4 (a) Selectivity analysis showing $\Delta\Delta G$ as a function of ΔG_{OH^*} for various investigated active sites in carbon-based materials and two-dimensional boron nitride. (b) Combined selectivity–activity map, where the highlighted green region indicates the optimal zone for both high selectivity and catalytic activity. The inset displays the atomic structure and highlights the active site (indicated by red circles) of the only structure that meets both the high activity and selectivity criteria. Labels *a* to *j* correspond to the reported values on various two-dimensional materials in the literature as reported in the SI. Error bars on data points show the individual uncertainties in each datapoint. (c) Bar chart highlighting the most promising two-dimensional structures exhibiting either $\Delta\Delta G \leq 0.65$ eV (indicated by the red dashed line) or $\eta_{2e\text{-}ORR} \leq 0.20$ V (indicated by the black dashed line). (d) Several examples of the atomic structures highlighted in pink and green in the bar chart. Red oval indicates the active site.

The pH of the electrolyte affects the chemical potential of protons and thereby the protonation states and surface coverage of adsorbed species, which can alter the relative free energies and shift selectivity patterns.[54,55] For example, changes in pH may modulate the favourability of proton–coupled electron transfer steps, impacting reaction rates and product distribution.[56] Alternatively, under alkaline conditions, cations are known to induce a field effect that particularly influences the adsorption energy of the *OOH intermediate.[57] Similarly, the solvent environment, especially water, plays a crucial role through hydrogen bonding and solvation effects that stabilize certain intermediates more than others.[46] Prior experimental and theoretical studies have demonstrated that intermediates such as *OH and *OOH are stabilized by explicit solvation, which can modify their adsorption energies compared to vacuum or implicit solvent models.[58]

Temperature further influences reaction thermodynamics by affecting entropy contributions and kinetic barriers, potentially altering both adsorption strengths and reaction selectivity.[59] Together, these factors create a complex, dynamic environment

that is difficult to fully capture within static DFT calculations using simplified models.

Therefore, while $\Delta\Delta G$ provides a valuable and computationally accessible baseline descriptor reflecting fundamental thermodynamic trends, it should be interpreted as part of a broader mechanistic context. We recommend that its predictions be complemented by more detailed studies incorporating explicit solvent models, pH-dependent proton activities, and temperature effects, either through computational approaches such as *ab initio* molecular dynamics or through careful experimental validation.

Despite these limitations, the $\Delta\Delta G$ descriptor remains an essential and practical starting point for screening and rational design of 2e-ORR electrocatalysts. It offers fundamental insights into intrinsic selectivity trends that are otherwise challenging to extract from purely experimental data. As such, it should continue to be routinely employed within the computational catalysis community to guide the discovery and optimization of new materials for sustainable electrochemical applications.

Conclusions

Advancing the discovery of novel materials for the electrosynthesis of hydrogen peroxide (H_2O_2) *via* the two-electron oxygen reduction reaction (2e-ORR) requires not only identifying catalytically active sites but also rationalizing their selectivity. The recently proposed thermodynamic descriptor, $\Delta\Delta G$, based on the adsorption free energies of key ORR intermediates (ΔG_{OOH*} and ΔG_{O*}) and H_2O_2, offers a valuable framework for quantifying selectivity and establishing design principles. While $\Delta\Delta G$ has shown strong predictive power in the context of metal alloys, its broader applicability to emerging materials such as carbon-based structures and boron nitrides remains a key question. In this study, we systematically evaluated a diverse set of active sites within these classes of materials and demonstrated that $\Delta\Delta G$ is effective in distinguishing sites that are both highly selective and catalytically active. Our results reveal that many sites reported to be active for 2e-ORR do not necessarily exhibit high selectivity, underscoring the need to consider both factors simultaneously in catalyst design. Among the structures investigated, only a small subset of sites—such as nitrogen-doped single vacancy defects—met both selectivity and activity criteria, highlighting promising directions for future development.

Conflicts of interest

There are no conflicts to declare.

Data availability

All data used in the analyses for this manuscript are provided in the SI.

The SI provides the calculated and compiled adsorption energies of ORR intermediates, along with the corresponding 2e-ORR overpotentials and selectivities. See DOI: https://doi.org/10.1039/d5sc04904k.

Acknowledgements

This work was supported by Natural Sciences and Engineering Research Council (NSERC) of Canada (Discovery Grant No. RGPIN-2023-05298). The contribution of Benedict Ly to data organization, carried out as part of an undergraduate research course at Simon Fraser University, is gratefully acknowledged.

References

1 J. M. Campos-Martin, G. Blanco-Brieva and J. L. G. Fierro, *Angew. Chem. Int. Ed. Engl.*, 2006, **45**, 6962–6984.
2 L. Lin, N. Miao, G. G. Wallace, J. Chen and D. A. Allwood, *Adv. Energy Mater.*, 2021, **11**, 1–22.
3 A. R. F. Pipi, I. Sirés, A. R. De Andrade and E. Brillas, *Chemosphere*, 2014, **109**, 49–55.
4 S. Siahrostami, A. Verdaguer-Casadevall, M. Karamad, D. Deiana, P. Malacrida, B. Wickman, M. Escudero-Escribano, E. a Paoli, R. Frydendal, T. W. Hansen, I. Chorkendorff, I. E. L. S. Stephens, I. E. Stephens and J. Rossmeisl, *Nat. Mater.*, 2013, **12**, 1137–1143.
5 J. K. Nørskov, J. Rossmeisl, A. Logadottir, L. Lindqvist, J. R. Kitchin, T. Bligaard and H. Jónsson, *J. Phys. Chem. B*, 2004, **108**, 17886–17892.
6 S. Siahrostami, S. J. Villegas, A. H. Bagherzadeh Mostaghimi, S. Back, A. B. Farimani, H. Wang, K. A. Persson and J. Montoya, *ACS Catal.*, 2020, **10**, 7495–7511.
7 S. C. Perry, D. Pangotra, L. Vieira, L.-I. Csepei, V. Sieber, L. Wang, C. Ponce de León and F. C. Walsh, *Nat. Rev. Chem.*, 2019, **3**, 442–458.
8 K. Wang, J. Huang, H. Chen, Y. Wang and S. Song, *Chem. Commun.*, 2020, **56**, 12109–12121.
9 A. Verdaguer-Casadevall, D. Deiana, M. Karamad, S. Siahrostami, P. Malacrida, T. W. Hansen, J. Rossmeisl, I. Chorkendorff and I. E. L. Stephens, *Nano Lett.*, 2014, **14**, 1603–1608.
10 H. W. Kim, M. B. Ross, N. Kornienko, L. Zhang, J. Guo, P. Yang and B. D. McCloskey, *Nat. Catal.*, 2018, **1**, 282–290.
11 L. Han, Y. Sun, S. Li, C. Cheng, C. E. Halbig, P. Feicht, J. L. Hübner, P. Strasser and S. Eigler, *ACS Catal.*, 2019, **9**, 1283–1288.
12 D. Iglesias, A. Giuliani, M. Melchionna, S. Marchesan, A. Criado, L. Nasi, M. Bevilacqua, C. Tavagnacco, F. Vizza, M. Prato and P. Fornasiero, *Chem*, 2018, **4**, 106–123.
13 Y. Sun, S. Li, Z. P. Jovanov, D. Bernsmeier, H. Wang, B. Paul, X. Wang, S. Kühl and P. Strasser, *ChemSusChem*, 2018, **11**, 3388–3395.
14 Y. Sun, L. Silvioli, N. R. Sahraie, W. Ju, J. Li, A. Zitolo, S. Li, A. Bagger, L. Arnarson, X. Wang, T. Moeller, D. Bernsmeier, J. Rossmeisl, F. Jaouen and P. Strasser, *J. Am. Chem. Soc.*, 2019, **141**, 12372–12381.
15 X. Hu, X. Zeng, Y. Liu, J. Lu and X. Zhang, *Nanoscale*, 2020, **12**, 16008–16027.

16 Z. Lu, G. Chen, S. Siahrostami, Z. Chen, K. Liu, J. Xie, L. Liao, T. Wu, Di. Lin, Y. Liu, T. F. Jaramillo, J. K. Nørskov and Y. Cui, *Nat. Catal.*, 2018, **1**, 156–162.
17 G.-F. Han, F. Li, W. Zou, M. Karamad, J.-P. Jeon, S.-W. Kim, S.-J. Kim, Y. Bu, Z. Fu, Y. Lu, S. Siahrostami and J.-B. Baek, *Nat. Commun.*, 2020, **11**, 2209.
18 X. Yan, W. W. Shi and X. Z. Wang, *New Carbon Mater.*, 2022, **37**, 223–236.
19 S. Chen, Z. Chen, S. Siahrostami, D. Higgins, D. Nordlund, D. Sokaras, T. R. Kim, Y. Liu, X. Yan, E. Nilsson, R. Sinclair, J. K. Norskov, T. F. Jaramillo and Z. Bao, *J. Am. Chem. Soc.*, 2018, **140**, 7851–7859.
20 K. Jiang, S. Back, A. J. Akey, C. Xia, Y. Hu, W. Liang, D. Schaak, E. Stavitski, J. K. Nørskov, S. Siahrostami and H. Wang, *Nat. Commun.*, 2019, **10**, 3997.
21 Y. Sun, S. Li, B. Paul, L. Han and P. Strasser, *J. Electroanal. Chem.*, 2021, **896**, 115197.
22 H. Zhao, Q. Jin, M. A. Khan, S. Larter, S. Siahrostami, M. G. Kibria and J. Hu, *Chem Catal*, 2022, **2**, 1720–1733.
23 F. Gui, Q. Jin, D. Xiao, X. Xu, Q. Tan, D. Yang, B. Li, P. Ming, C. Zhang, Z. Chen, S. Siahrostami and Q. Xiao, *Small*, 2022, **18**, 2105928.
24 F. Gui, Q. Jin, D. Xiao, Z. Jin, Y. Zhang, Y. Cao, M. Yang, Q. Tan, C. Zhang, S. Siahrostami and Q. Xiao, *J. Mater. Chem. A*, 2023, **11**, 1312–1323.
25 J. W. F. To, J. W. D. Ng, S. Siahrostami, A. L. Koh, Y. Lee, Z. Chen, K. D. Fong, S. Chen, J. He, W.-G. Bae, J. Wilcox, H. Y. Jeong, K. Kim, F. Studt, J. K. Nørskov, T. F. Jaramillo and Z. Bao, *Nano Res.*, 2017, **10**, 1163–1177.
26 Y. Song, C. Hu, C. Li and X. Xu, *J. Phys. Chem. C*, 2024, **128**, 5590–5596.
27 J. Jia, Z. Li, Y. Tian, X. Li, R. Chen, J. Liu and J. Liang, *Energy Rev.*, 2024, **3**, 100069.
28 K. Mase, M. Yoneda, Y. Yamada and S. Fukuzumi, *ACS Energy Lett.*, 2016, **1**, 913–919.
29 D. Cao, J. Chao, L. Sun and G. Wang, *J. Power Sources*, 2008, **179**, 87–91.
30 X. Long, Y. Ling, C. Chang, F. Luo and Z. Yang, *Chem. Commun.*, 2022, **58**, 9782–9785.
31 S. Chen, Z. Chen, S. Siahrostami, T. R. Kim, D. Nordlund, D. Sokaras, S. Nowak, J. W. F. To, D. Higgins, R. Sinclair, J. K. Nørskov, T. F. Jaramillo and Z. Bao, *ACS Sustain. Chem. Eng.*, 2018, **6**, 311–317.
32 Q. Chang, P. Zhang, A. H. B. Mostaghimi, X. Zhao, S. R. Denny, J. H. Lee, H. Gao, Y. Zhang, H. L. Xin, S. Siahrostami, J. G. Chen and Z. Chen, *Nat. Commun.*, 2020, **11**, 2178.
33 K. Jiang, S. Siahrostami, A. J. Akey, Y. Li, Z. Lu, J. Lattimer, Y. Hu, C. Stokes, M. Gangishetty, G. Chen, Y. Zhou, W. Hill, W.-B. Cai, D. Bell, K. Chan, J. K. Nørskov, Y. Cui and H. Wang, *Chem*, 2017, **3**, 950–960.
34 Y. Sun, I. Sinev, W. Ju, A. Bergmann, S. Dresp, S. Kühl, C. Spöri, H. Schmies, H. Wang, D. Bernsmeier, B. Paul, R. Schmack, R. Kraehnert, B. Roldan Cuenya and P. Strasser, *ACS Catal.*, 2018, **8**, 2844–2856.
35 B. Kumar, M. Asadi, D. Pisasale, S. Sinha-Ray, B. A. Rosen, R. Haasch, J. Abiade, A. L. Yarin, A. Salehi-Khojin, S. J. Davis, K. Caldeira, *et al.*, *Nat. Commun.*, 2013, **4**, 1330–1333.
36 K. Dong, Y. Lei, H. Zhao, J. Liang, P. Ding, Q. Liu, Z. Xu, S. Lu, Q. Li and X. Sun, *J. Mater. Chem. A*, 2020, **8**, 23123–23141.
37 S. Siahrostami, *Chem Catal*, 2023, **3**, 100568.
38 S. Yang, A. Verdaguer-Casadevall, L. Arnarson, L. Silvioli, V. Čolić, R. Frydendal, J. Rossmeisl, I. Chorkendorff and I. E. L. Stephens, *ACS Catal.*, 2018, **8**, 4064–4081.
39 G. Chen, J. Liu, Q. Li, P. Guan, X. Yu, L. Xing, J. Zhang and R. Che, *Nano Res.*, 2019, **12**, 2614–2622.
40 D. H. Mok, S. Back and S. Siahrostami, *Angew. Chem. Int. Ed.*, 2024, **63**, e202404677.
41 A. Hjorth Larsen, J. Jørgen Mortensen, J. Blomqvist, I. E. Castelli, R. Christensen, M. Dułak, J. Friis, M. N. Groves, B. Hammer, C. Hargus, E. D. Hermes, P. C. Jennings, P. Bjerre Jensen, J. Kermode, J. R. Kitchin, E. Leonhard Kolsbjerg, J. Kubal, K. Kaasbjerg, S. Lysgaard, J. Bergmann Maronsson, T. Maxson, T. Olsen, L. Pastewka, A. Peterson, C. Rostgaard, J. Schiøtz, O. Schütt, M. Strange, K. S. Thygesen, T. Vegge, L. Vilhelmsen, M. Walter, Z. Zeng and K. W. Jacobsen, *J. Phys. Condens. Matter*, 2017, **29**, 273002.
42 P. Giannozzi, S. Baroni, N. Bonini, M. Calandra, R. Car, C. Cavazzoni, D. Ceresoli, G. L. Chiarotti, M. Cococcioni, I. Dabo, A. Dal Corso, S. de Gironcoli, S. Fabris, G. Fratesi, R. Gebauer, U. Gerstmann, C. Gougoussis, A. Kokalj, M. Lazzeri, L. Martin-Samos, N. Marzari, F. Mauri, R. Mazzarello, S. Paolini, A. Pasquarello, L. Paulatto, C. Sbraccia, S. Scandolo, G. Sclauzero, A. P. Seitsonen, A. Smogunov, P. Umari and R. M. Wentzcovitch, *J. Phys. Condens. Matter*, 2009, **21**, 395502.
43 K. T. Lundgaard, J. Wellendorff, J. Voss, K. W. Jacobsen and T. Bligaard, *Phys. Rev. B*, 2016, **93**, 235162.
44 J. Wellendorff, T. L. Silbaugh, D. Garcia-Pintos, J. K. Nørskov, T. Bligaard, F. Studt and C. T. Campbell, *Surf. Sci.*, 2015, **640**, 36–44.
45 A. I. M. Albashir, X. Lu, X. Dai and W. Qi, *Commun. Chem.*, 2024, **7**, 111.
46 V. J. Bukas, H. W. Kim, R. Sengpiel, K. Knudsen, J. Voss, B. D. McCloskey and A. C. Luntz, *ACS Catal.*, 2018, **8**, 11940–11951.
47 K. H. Koh, Y. J. Kim, A. H. B. Mostaghim, S. Siahrostami, T. H. Han and Z. Chen, *ACS Mater. Lett.*, 2022, **4**, 320–328.
48 K. Liu, J. Fu, Y. Lin, T. Luo, G. Ni, H. Li, Z. Lin and M. Liu, *Nat. Commun.*, 2022, **13**, 2075.
49 X. Li, Z. Wang, Z. Su, Z. Zhao, Q. Cai and J. Zhao, *ChemPhysMater*, 2022, **1**, 237–245.
50 J.-K. Sun, Y.-W. Pan, M.-Q. Xu, L. Sun, S. Zhang, W.-Q. Deng and D. Zhai, *Nano Res.*, 2024, **17**, 1086–1093.
51 J. Kaur, V. Sharma, D. Kumar Das, B. Pandit, M. Shahzad Samdani, M. Shkir, M. Aslam Manthrammel, S. Nangan, V. Jagadeesha Angadi and M. Ubaidullah, *Fuel*, 2024, **358**, 130241.
52 Z. Hou, X. Wang, T. Ikeda, K. Terakura, M. Oshima, M. Kakimoto and S. Miyata, *Phys. Rev. B:Condens. Matter Mater. Phys.*, 2012, **85**, 165439.

53 R. Urrego-ortiz, M. O. Almeida and F. Calle-vallejo, *ChemSusChem*, 2024, **17**, e202400873.
54 H. A. Hansen, J. Rossmeisl and J. K. Nørskov, *Phys. Chem. Chem. Phys.*, 2008, **10**, 3722.
55 M. F. Li, L. W. Liao, D. F. Yuan, D. Mei and Y.-X. Chen, *Electrochim. Acta*, 2013, **110**, 780–789.
56 M. T. M. Koper, *Chem. Sci.*, 2013, **4**, 2710.
57 S. R. Kelly, C. Kirk, K. Chan and J. K. Nørskov, *J. Phys. Chem. C*, 2020, **124**, 14581–14591.
58 H. Zhao, X. Lv and Y.-G. Wang, *Adv. Sci.*, 2023, **10**, e2303677.
59 I. Roche and K. Scott, *J. Electroanal. Chem.*, 2010, **638**, 280–286.